Materials and Design 174 (2019) 107790

Contents lists available at ScienceDirect

Materials and Design

journal homepage: www.elsevier.com/locate/matdes

Extrudable hydroxyapatite/plant oil-based biopolymer nanocomposites for biomedical applications: Mechanical testing and modeling

Aram Bahmani [a,b], Patricia A. Comeau [b], John Montesano [a], Thomas L. Willett [b,*]

[a] Composites Research Group, Department of Mechanical and Mechatronics Engineering, University of Waterloo, 200 University Ave. West, Waterloo N2L 3G1, Canada
[b] Composite Biomaterial Systems Laboratory, Department of Systems Design Engineering, University of Waterloo, 200 University Ave. West, Waterloo N2L 3G1, Canada

HIGHLIGHTS

- Two extrudable nanocomposites of soybean oil epoxidized acrylate and silanized nano-hydroxyapatite were produced.
- The biopolymer resins and 3D-printed nanocomposite filaments were characterized using TGA and SEM.
- Mechanical performance of both resins and extruded nanocomposite filaments was assessed using small-scale tensile tests.
- 3D finite element micromechanical models were developed to investigate orthotropic responses of the nanocomposite filaments.
- Experimental data were compared with results from finite element and analytical micromechanical models.

GRAPHICAL ABSTRACT

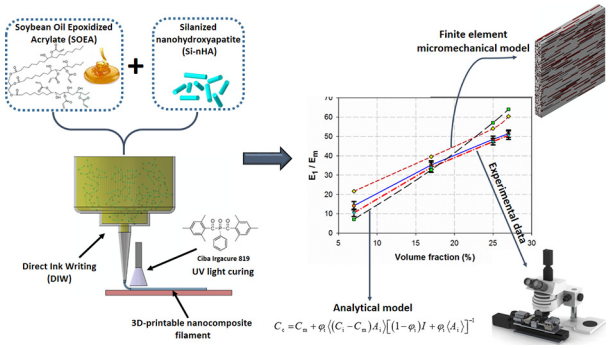

ARTICLE INFO

Article history:
Received 19 February 2019
Received in revised form 7 April 2019
Accepted 8 April 2019
Available online 12 April 2019

Keywords:
Nanocomposites
Nano-hydroxyapatite
Soybean oil epoxidized acrylate
Bone-inspired materials
Micromechanical modeling
Filament tensile testing

ABSTRACT

Towards developing bone-inspired, high performance composite biomaterials, two nanocomposite inks, consisting of a plant oil-based biopolymer resin (soybean oil epoxidized acrylate (SOEA)) and silanized nano-hydroxyapatite (Si-nHA) particles with and without diluent hydroxyethyl acrylate (HEA), were extruded using direct ink writing to fabricate filaments of differing volume fractions. HEA was hypothesized to lower ink viscosity, improve Si-nHA dispersion and extrudability, and therefore result in better relative improvements in mechanical properties over those of the base resin. Thermogravimetric analysis, scanning electron microscopy and uniaxial tensile tests were conducted. Strength, toughness, and stiffness of both resins were improved by the addition of Si-nHA. The HEA improved dispersion and extrudability. This resulted in better particle alignment and relatively greater augmentation of mechanical properties. The experimental data for both biopolymer resins were used to calibrate 3D representative volume element (RVE) finite element micromechanical models, while the experimental data for the nanocomposite filaments were employed to validate these models. The Young's moduli from the computational models were also compared with experimental data and with analytical predictions calculated using the Mori-Tanaka method. The predictions of 3D RVE models correlated well with the experimental data while, for higher volume fractions, the Mori-Tanaka results diverged, similar to previous reports.

* Corresponding author.
E-mail address: Thomas.willett@uwaterloo.ca (T.L. Willett).

https://doi.org/10.1016/j.matdes.2019.107790

1. Introduction

Biological and natural materials, such as cortical bone, demonstrate high-performance in terms of mechanical properties including the advantageous combination of a high specific strength and toughness. Cortical bone is composed of approximately 45% by-volume (vol%) stiff hydroxyapatite nanocrystals embedded in approximately 45 vol% compliant collagen fibrils and proteins arranged in sophisticated hierarchical architectures at different length scales [1,2]. The remaining 10 vol% is attributed to an aqueous phase and porosity [1,2]. The mechanical performance of bone grafts and current synthetic biomaterials used to repair bone (such as bone cements) require improvement [5]. For this purpose, various factors including chemical composition, nano/microstructure, and hierarchy architecture can be inspired from bone itself [6].

To design and fabricate bone-inspired composite materials, a wide range of polymers, inclusions and fabrication techniques have been investigated [7–10]. Examples of these fabrication techniques include: 3D-printing [7], magnetic alignment [7,8], magnetically assisted slip casting [8,9], and robocasting [10], among others. Achieving ~45 vol% of the reinforcing mineral particles within a discontinuous composite material is a significant challenge due to limitations with these fabrication process [3–12]. Several types of bone-inspired biocomposites have been proposed, including fiber-reinforced non-degradable composites [13,14], nanoparticulate non-degradable composites [13,14], partially and entirely degradable fiber-reinforced composites [13,14], inorganic filler-reinforced composites with degradable matrix [13,14], and nanoparticulate degradable composites [13,14]. To the best of our knowledge, the mechanical properties of these materials are far inferior to those of cortical bone. For instance, similar levels of stiffness, toughness, and strength have not simultaneously been achieved [13,14]. In addition, the matrix of previously reported bioinspired composites was reinforced using micro-scale, continuous, and non-staggered nano-scale particles [13,14]. To date, the use of nano-scale inclusions ('nanoparticles') has been limited due to difficulty in handling and arranging them into a bone-like staggered structure and minimizing particle agglomeration [5–7,11–14]. Although it seems currently impossible to generate a low density high-performance material (i.e., having simultaneous high specific stiffness, toughness and strength) with nano-scale staggered structure similar to bone, it is quite essential to tackle this topic because these types of high-performance materials not only can be applied for biomedical applications but also other industrial applications.

Recently, the utilization of vegetable oil-based polymers (VOBPs) for generating synthetic biomaterials has received significant attention due to their universal accessibility, renewability, intrinsic biodegradability and biocompatibility, as well as their low cost [15–18]. One intriguing plant oil monomers is soybean oil epoxidized acrylate (SOEA). This material can be cross-linked (cured) using UV light following the addition of a photoinitiator such as bis (2,4,6-trimethylbenzoyl)-phenylphosphineoxide [17]. Miao et al. [17] employed SOEA to generate several bio-polymeric scaffolds using '4D printing'. They also investigated SOEA's cytocompatibility. They found that SOEA is cytocompatible and also appropriate for 4D-printing. In order to fabricate bone-inspired composites, various biocompatible polymers such as gelatin [19,20], chitosan [21], polylactic-co-glycolic acid (PLGA) [22], and polyetheretherketone (PEEK) [23,24] have been reinforced using nano-hydroxyapatite (nHA) particles with mixed results. To the best of our knowledge, this current work is the first report on the fabrication of a staggered structure compositing a plant oil derived biopolymer, like SOEA, with nHA for bone-inspired composites.

Characterization of bone-inspired nanocomposites having complex staggered structural arrangements and indeed, the establishment of general design guidelines, is pivotal for widespread adoption of these materials. To facilitate this, it is essential to develop robust high-fidelity design tools to predict the performance of bone-inspired composites. Micromechanical finite element (FE) modeling provides an efficient means to conduct virtual experiments for various materials systems during design, while at the same time allowing for greater flexibility with regards to assessing material nonlinearities, phase interactions and local damage progression of bone-inspired composites. Several FE micromechanical models have been proposed to characterize staggered or aligned discontinuous inclusion-reinforced composites [25–31]. Here, overall microstructure, effects of the tri-axial state of stress, inclusion shape, and boundary conditions are often simplified and are not an accurate representation of the material [25–31]. Recently, Bahmani et al. [32] proposed two novel and efficient 3D staggered FE micromechanical models for assessing the performance of various biomimetic/bioinspired composite materials with different inclusion shapes and sizes.

In this current study, two SOEA-based biopolymers are reinforced using nHA particles to create two new bone-inspired nanocomposites. Scanning electron microscopy (SEM), and thermogravimetric analyses (TGA) were used to characterize these nanocomposite materials. In addition, a number of dog-bone-shaped specimens of both biopolymers were tensile tested in order to employ that data in computational models (from Bahmani et al. [32]). Both nanocomposites were extruded as filaments and tensile tested. Lastly, the computational models from Bahmani et al. [32] were validated and compared with experimental data from the aforementioned extruded nanocomposite filaments and the well-established analytical Mori-Tanaka model. One hypothesis for this study was that the use of the HEA diluent would lower ink viscosity (by acting as a lower molecular weight diluent), improve dispersion and extrudability (through altering hydrogen bonding with the nHA), and this would result in better particle alignment and relatively greater augmentation of mechanical properties (stiffness and strength especially; relative to unfilled and lower volume fraction inks of the same base resin).

2. Experimental methods

2.1. Nano-hydroxyapatite characterization and functionalization

One of the crucial parameters in determining the mechanical performance of a composite is the inclusion/particle shape. In this study, rod-shaped nano-hydroxyapatite (nHA) particles (MK Nano, Mississauga, Canada) were employed. Comeau and Willett [33] previously reported on the characteristics of this nHA powder, which was found to have a crystallinity of 66%, a Ca/P ratio of 1.5 and is rod shaped with a ~120 nm length and 20–30 nm width on average. In addition, ATR-FTIR of the nHA has confirmed its carbonated nature [33]. Finally, the density of these nHA particles was confirmed to be 2.9 g/cm^3.

A silanization process was performed on the nHA particles to improve interfacial bonding between the nano-particles and SOEA resin [34]. In this study, we chose silanization to provide a covalent bonding interface, which would best approximate the perfect interface assumed in our computational models [32]. Silanized nano-hydroxyapatite (Si-nHA) has previously been found to create more bone apposition at the surface of implants and improve bioactivity than un-modified nHA [35–39].

A solvent mixture of 90 vol% ethanol (EtOH) and 10 vol% deionized water (dH2O) was prepared in a 250 mL glass beaker with stirring on a horizontal stir plate (VWR) at 200–300 rpm. Next, 3 methacryloxypropyltrimethoxysilane (MPTS) was added to the EtOH solvent mixture to obtain a solution with 5 vol% MPTS. The pH of the MPTS-solvent mixture was then adjusted to 4 using 3.0 M acetic acid and was monitored using a pH meter (Accumet, Fisher Scientific). The buffered MPTS-solvent mixture was then covered with plastic wrap and stirred for 1 h to hydrolyze (i.e., activate). Then, the MPTS-solvent mixture was added to 10 g of the nHA powder in a 1 L capped glass container and sonicated for 15 min in a water bath (Symphony, VWR) at 50

°C. After sonication, the nHA/MPTS-solvent suspension was stirred for 24 h at room temperature on a horizontal stir plate (VWR) at 200–300 rpm. The nHA/MPTS-solvent suspension was then dialyzed using dialysis tubing with a 13 kDa cut-off in a dH2O bath for 1 h. Following dialysis, the Si-nHA powder was recovered by drying the dialyzed mixture for 3 days at room temperature in a fume hood (see [35] for more details).

2.2. Preparation of inks

One of the main obstacles to achieving high Si-nHA volume fractions is the high viscosity of plant oil based resins, like SOEA. To overcome this problem of high viscosity in other resin systems, Wozniak et al. [40,41] employed additional diluent monomers such as 2-hydroxyethyl acrylate (HEA). Owing to this prior success, here we have also used HEA. The first composite was composed of Si-nHA and SOEA alone, while the second consisted of Si-nHA and an equal volume mixture of SOEA and HEA. For the first ink, 10 g Si-nHA was mixed with 30 mL EtOH using an ultrasonic homogenizer (Branson Sonifier 450 Analog) for 3 min. A solvent mixture of SOEA and 10 mL EtOH was similarly prepared using the ultrasonic homogenizer for 2 min. Before final mixing of the Si-nHA/EtOH with the SOEA/EtOH, the Si-nHA/EtOH mixture was homogenized again for 1 min then added to SOEA/EtOH and the final solvent homogenized for 1 min. Next, the container was loosely covered with aluminum foil and the EtOH allowed to evaporate in a fume hood. During EtOH evaporation and drying to a constant weight, the solvent mixture was homogenized each day for 2 min. For the second ink, again 10 g Si-nHA was mixed with 30 mL EtOH using an ultrasonic homogenizer for 3 min. A solvent mixture of 50 vol% SOEA and 50 vol% HEA was prepared and then homogenized with 10 mL EtOH using the ultrasonic homogenizer for 2 min. All other steps were similar to the first composition. After drying and EtOH evaporation for 3 days, 1.26% Ciba Irgacure 819 was dissolved in acetone and then added to both inks using the ultrasonic homogenizer for 2 min. Eventually, two resins (i.e., Si-nHA/SOEA and Si-nHA/SOEA + HEA) were prepared, and we produced four inks from each with each ink having different Si-nHA volume fractions (10%, 20%, 30%, and 40% target values). Table 1 provides more details about the matrix and nanoparticle ('inclusion') phase volume fraction for each nanocomposite ink.

2.3. Direct ink writing

In order to produce nanocomposite filaments, an extrusion-based 3D-printing method termed direct ink writing (DIW) was used. The 3D printer was a System 30 M (Hyrel, Georgia, USA) equipped with a Volcano print head. To tailor the mechanical performance of these nanocomposites, non-uniformly dispersed particles in a staggered or aligned structure were required. Indeed, high shear stresses in a nozzle can drive nHA particle alignment. By decreasing the nozzle tip diameter and increasing feed rate, shear stress can be increased [11,12]. Therefore, the conical shape nozzle with two tip diameters (D_n) (0.26 mm and 0.41 mm) was chosen. Also, 1000 mm/min 3D-printing speed was applied, and the distance between build plate and the nozzle tip was manually adjusted in order to achieve consistent filaments.

2.4. Nanocomposite characterizations

In order to assess the dispersion and alignment of nanoparticles in the ink, scanning electron microscopy (SEM) was performed. The SEM (Zeiss FESEM 1530) instrument was used with an electron high tension (EHT) value of 10 kV, three different magnifications of 10, 25, and 50 KX, a working distance range from 7 to 9 mm relative to size of specimen, and two types of detectors (SE2 and InLens). In addition, Thermo-Gravimetric Analysis (TGA) was conducted on the UV-cured filaments to determine the actual volume fraction of nHA in each nanocomposite. Samples were heated to 800 °C at a rate of 10 °C/min ($n = 3$).

2.5. Specimen preparation for biopolymer resin tensile tests

Mechanical tests on SOEA and SOEA + HEA resin specimens were performed in order to define their tensile mechanical properties for the FE micromechanical models (additional detail in Section 3), and to compare their respective mechanical properties. A Teflon dog-bone mold was used for fabrication of the test specimens, which were cured using a broad wavelength range UV light box (1 mW/cm^2 at 385 nm; SHANY®). For the purpose of preparing both biopolymer dog-bone specimens, first, 1.26% Ciba Irgacure 819 was added to acetone at a concentration of 1% and then homogenized with the SOEA using the ultrasonic homogenizer for 2 min. The same amount of Ciba Irgacure 819 and Acetone was mixed together with the ultrasonic homogenizer for 2 min upon addition to the SOEA + HEA resin. After the acetone evaporation, both resins (i.e., SOEA and SOEA + HEA) were stored in capped plastic tubes in a water bath at ~40 °C for at least 1 h to eliminate air bubbles. A glass microscope slide was then attached to one side of the mold using vacuum grease and then a 5 mL syringe was used to add the resin to the molds, before UV curing for 320 min.

2.6. Filament test specimen preparation

Conducting uniaxial tensile tests on extruded filaments is challenging due to the limitation of fixtures and testing machines at this small scale. Here, a new method was employed to ensure sample stability while testing. First, trapezoidal tabs similar to the head of the dog-bone specimens discussed above were 3D-printed using poly lactic acid (PLA) on a Lulzbot Mini 3D Printer (Aleph Objects, Colorado, USA). The length of filaments were 50 ± 10 mm; hence, in order to bind the filaments within the tabs, superglue (Gorilla Super Glue, The Gorilla Glue Co., Ohio, USA) was used, as depicted in Fig. 1, and allowed to cure for 24 h.

2.7. Micro-mechanical tensile tests

Uniaxial tensile tests on resin dog-bone specimens and nanocomposite filaments were conducted using a small universal testing machine (μTS, Psylotech, Evanston, IL, USA) integrated with an optical microscope (BXFM, Olympus, Toronto, ON, Canada) and digital camera, which together enabled 2D digital image correlation (DIC) for strain measurement [42] (See Fig. 2). The commercial VIC-2D software package (Correlated Solutions Inc., Irmo, SC, USA) was used to calculate engineering stain from the digital images using the DIC method [42]. Both the dog-bone specimens and nanocomposite filaments were tested at a

Table 1
The target volume fractions of resin and inclusion phase in each nanocomposite ink.

Si-nHA/SOEA ink		Si-nHA/SOEA + HEA ink	
Matrix phase (vol%)	Inclusion phase (vol%)	Matrix phase (vol%)	Inclusion phase (vol%)
SOEA 90%	Si-nHA 10%	SOEA 45% + HEA 45%	Si-nHA 10%
SOEA 80%	Si-nHA 20%	SOEA 40% + HEA 40%	Si-nHA 20%
SOEA 70%	Si-nHA 30%	SOEA 35% + HEA 35%	Si-nHA 30%
SOEA 60%	Si-nHA 40%	SOEA 30% + HEA 30%	Si-nHA 40%

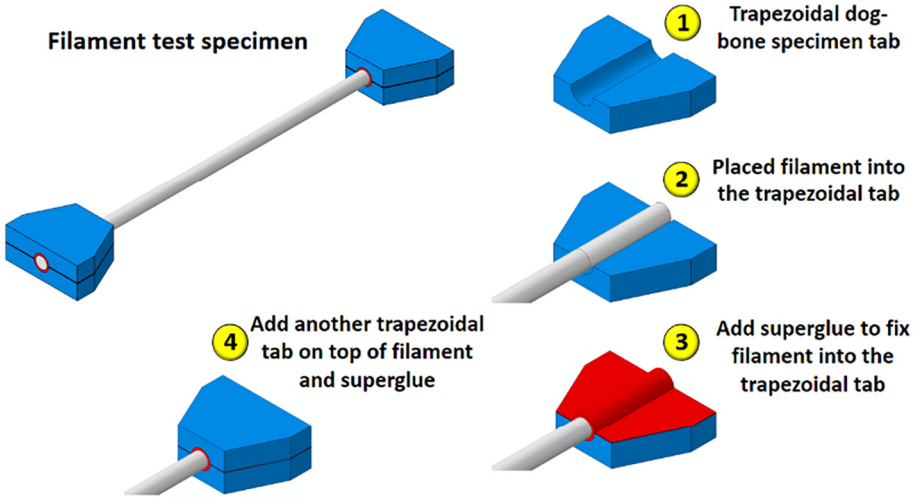

Fig. 1. Nanocomposite filament test specimen configuration and preparation process.

constant rate of 1 mm/min. The spatial resolution using the 5× lens of the Olympus microscope was 0.000688 mm/pixel. DIC images were acquired as 5 frames per second, and the analysis used a subset size of 29 pixels, a step size of 7, and a strain filter of 15 pixels. Note that for each nanocomposite filament group and biopolymer dog-bone sample group, five specimens were tested.

3. Micromechanical simulations

In order to compute the orthotropic elastic constants of the extruded nanocomposite filaments, periodic 3D micromechanical finite element models with non-uniformly dispersed staggered and aligned inclusions can be an accurate and reliable computational tool. Recently, Bahmani et al. [32] proposed such models for this purpose and the authors employed them herein. In these models, a custom 3D Staggered Hard-Core algorithm (SHCA) was used to generate the coordinates of non-uniformly dispersed staggered and aligned inclusions in periodic 3D representative volume elements (RVEs). The generated RVE coordinates were used to create the corresponding volumes in ABAQUS (version 6.14) using custom PYTHON algorithms. The non-uniform spatial distribution of the staggered inclusions within the generated RVEs was assessed using 3D spatial analysis functions, namely 3D autocorrelation analysis (see [43,44] for more details). These analyses demonstrated that the generated 3D RVEs have consistent non-uniformly distributed inclusions [32,43,44].

For the present study, based on thermogravimetric analyses results presented in Section 4, four inclusion volume fractions for each nanocomposite ($V_{i(\text{Si-nHA/SOEA})} = 10, 20, 25, 30$) and ($V_{i(\text{Si-nHA/SOEA+HEA})} = 7, 17, 25, 27$) with aspect ratio ($\rho$) of 4 were explored for cylindrical inclusion RVE models. The length, width, and height of 3D RVE are 400, 200, and 200 nm. Note that these chosen dimensions for 3D RVEs were based on a sensitivity analysis and have been compared with experimental data previously [32]. The inclusion and surrounding matrix material was assumed to be perfectly bonded. In order to apply periodic boundary conditions (PBCs) for these complex 3D RVEs, a previously developed dummy element and copy mesh technique was used (see Refs. [32,45] for more details). In the copy mesh method, only tetrahedral elements with a diminutive seed size can be used. Hence, C3D4 elements with sizes less than 1/10th of the cylindrical inclusion diameter and hexagonal platelet thickness were employed. Two different models were employed for both 3D-printed nanocomposite inks. Isotropic linear elastic properties were designated for both inclusions and matrix. The elastic properties for the matrix material were taken from the biopolymer tensile test results from Section 4. The Young's modulus and Poisson's ratio of the nHA inclusions were assigned as $E_{\text{nHA}} = 114$ GPa, $\nu_{\text{nHA}} = 0.27$ [46].

For the purpose of computing the bulk elastic mechanical properties of the inhomogeneous bone-inspired nanocomposites using the 3D RVEs generated as given above, a homogenization process utilizing volume averaged stresses and strains and 3D elastic equations was employed (see Refs. [32,45] for more details). In this study, the elastic constants were computed numerically by imposing a prescribed displacement (i.e., 0.5% strain) to the corresponding RVE surface. Normal and shear deformation was considered along all material directions to calculate the elastic constants (see Fig. 3). The corresponding results are presented in Section 4.

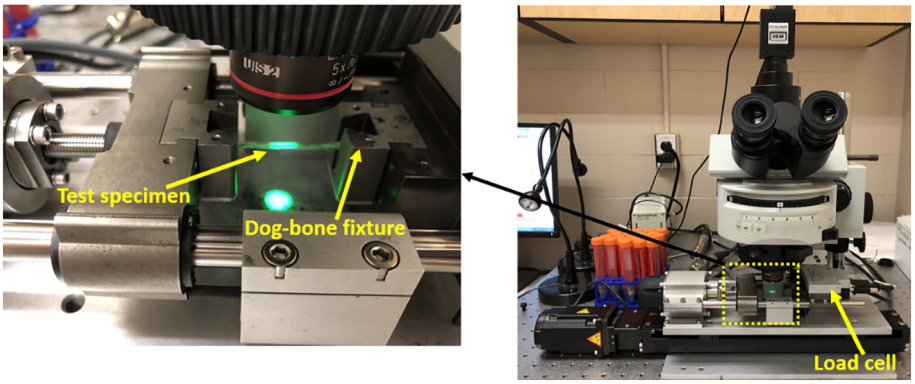

Fig. 2. Mechanical test configuration including a small-scale universal testing machine integrated with a microscope-based 2D DIC strain field measurement system.

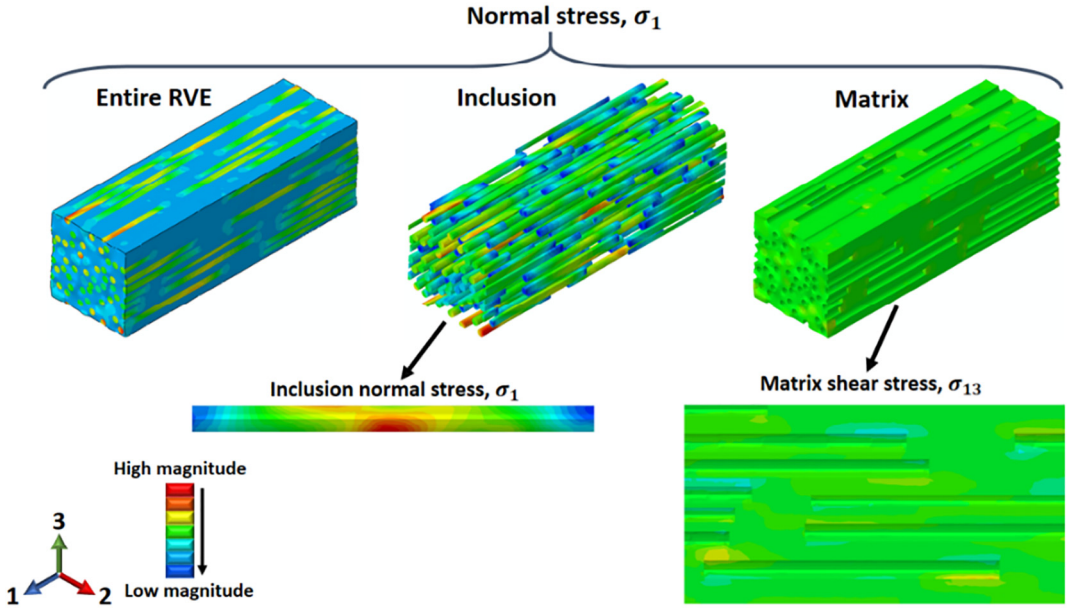

Fig. 3. Normal stress contours for a rod-like inclusion RVE model with uniaxial load applied in the 1-direction and demonstrating the shear-lag behavior in the inclusions and the matrix.

In Section 4, the results of this 3D RVE model are compared to an established analytical model. The Mori–Tanaka model can predict the elastic stiffness tensor of a composite material with assumed elliptical inclusions and interaction among inclusions and matrix using [47,48]:

$$C_c = C_m + \varphi_i \langle (C_i - C_m) A_i \rangle [(1-\varphi_i) I + \varphi_i \langle A_i \rangle]^{-1} \quad (1)$$

where C_c, C_m, and C_i are stiffness tensors of the composite, matrix, and inclusion respectively. φ_i is the inclusion volume fraction, I is the fourth order unit tensor, and A_i is the dilute mechanical strain concentration which can be expressed as follows:

$$A_i = \left[I + S(C_m)^{-1} (C_i - C_m) \right]^{-1} \quad (2)$$

The elements of Eshelby's tensor S are functions of inclusion aspect ratio (ρ) and matrix Poison's ratio (ν_m), which are presented in Appendix A.

4. Results and discussion

In this section, results from the nanocomposite material characterizations are presented. Experimental results for the resin dog-bone specimens and extruded nanocomposite filaments are also reported. The numerical results computed using the 3D RVE FE models and constituent properties are subsequently presented and compared with experimental and analytical results.

4.1. Filament characterization

Fig. 4(a–b) demonstrate the thermal decomposition and weight loss (%) of each batch versus temperature (°C). Table 2 reports the anticipated Si-nHA volume fractions during ink preparation versus actual Si-nHA volume fractions in extruded filaments determined by TGA.

In both nanocomposites, with increasing Si-nHA content, the differences between the target and the obtained Si-nHA volume fractions tended to increase. Reasons for these differences may include: 1) distinct

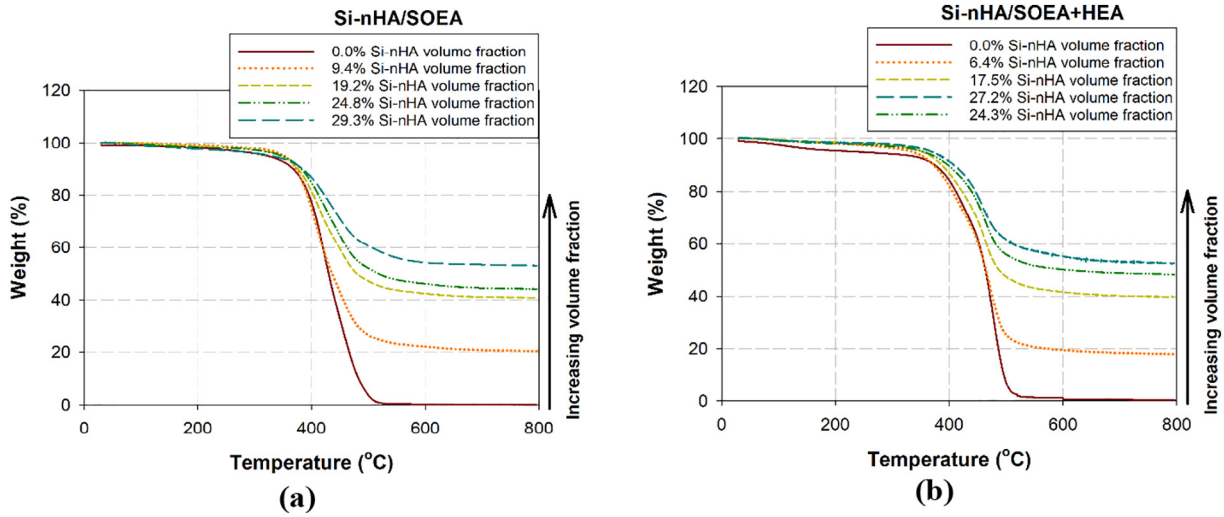

Fig. 4. Thermo-Gravimetric Analysis (TGA) data for both nanocomposites at different Si-nHA volume fractions. (a) Si-nHA/SOEA ink and (b) Si-nHA/SOEA + HEA ink.

Table 2
Comparisons between anticipated and actual Si-nHA volume fractions for each nanocomposite ink.

Si-nHA/SOEA		Si-nHA/SOEA + HEA	
Anticipated (vol%)	Determined by TGA (vol%)	Anticipated (vol%)	Determined by TGA (vol%)
10%	9.4%	10%	6.4%
20%	19.2%	20%	17.5%
30%	24.4%	30%	24.3%
40%	29.3%	40%	27.2%

differences in the viscosities of the resins and their non-covalent interactions with the Si-nHA, 2) filtration of the particles during extrusion and 3) simple experimental variations during ink preparation. TGA was performed so that the true volume fractions would be known and could be used in the FE and analytical micromechanical models.

Fig. 5 shows three different regions of a 17% Si-nHA/SOEA + HEA nanocomposite filament cross-section wherein SEM images were captured to assess the Si-nHA particle dispersion and alignment. The presence of what appears to be the circular cross-section of the nHA rods indicates alignment of the particles. In regions 1 and 3, no large agglomerations are obvious. These regions are closer to the outer surfaces of filament where higher shear stresses occur; however, in region 2, which is in the middle of filament where lower shear stresses are experienced, there are several small clusters.

4.2. Experimental data

The Young's modulus and Poisson's ratio of SOEA and SOEA + HEA were determined to be (based on mechanical testing) $E_{SOEA} = 81$ MPa and $\nu_{SOEA} = 0.45$, and $E_{SOEA+HEA} = 11$ MPa and, respectively.

Fig. 6(a) demonstrates representative engineering stress-strain curves for all of the materials tested in this study. One can visually compare the mechanical performance of both nanocomposites for all Si-nHA volume fractions tested. Clearly, the strength and toughness of the SOEA resin are notably greater than those of the SOEA + HEA resin. The most impressive batch in all these experiments is 17%Si-nHA/SOEA + HEA for two reasons, including (i) the toughness and strength are greatly increased relative to the unfilled SOEA + HEA resin, and (ii) both of these mechanical properties are higher or at least equal to 20%Si-nHA/SOEA ink, even though the Young's modulus of SOEA + HEA is approximately 11 MPa and this value for SOEA is around 81 MPa (see Table 3). Based on the SEM images shown in Fig. 5, this ink (17%Si-nHA/SOEA + HEA) benefits from excellent nanoparticle dispersion and alignment in all three regions. There are no clusters, and the nanoparticles, particularly in region 1 and 3, are more aligned. These regions are close to the outer surfaces of filament; however, in region 2, which is in the middle of filament, some relatively misaligned nanoparticles can be observed.

In Fig. 6(b), the engineering stresses shown in Fig. 6(a) are normalized to the ultimate tensile strength of their respective resin matrix. As can be seen, by increasing the Si-nHA volume fraction in the SOEA ink, the strength of material tends to be enhanced (by ~5×); however, by increasing Si-nHA volume fraction in SOEA + HEA ink, the strength of material improved greatly (~15×), and the toughness, particularly in 17% Si-nHA/SOEA + HEA, is remarkably increased. Based on these

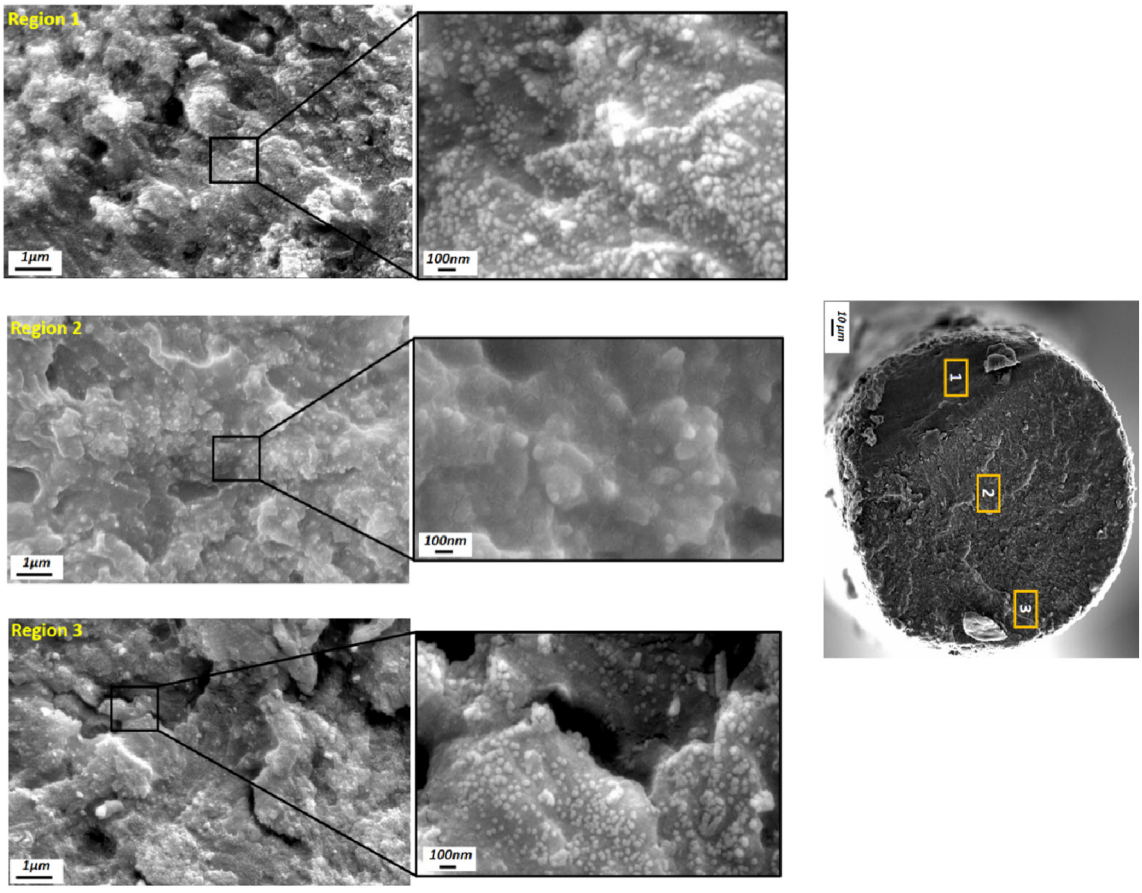

Fig. 5. Si-nHA nanoparticle dispersion and alignment as observed in SEM images of the extruded 17% Si-nHA/SOEA + HEA nanocomposite at the three different regions of the filament's cross-section. The dispersion and alignment of nanoparticles in the outer regions (i.e., region 1 and 3) are different from those found in region 2 (at the middle of the filament).

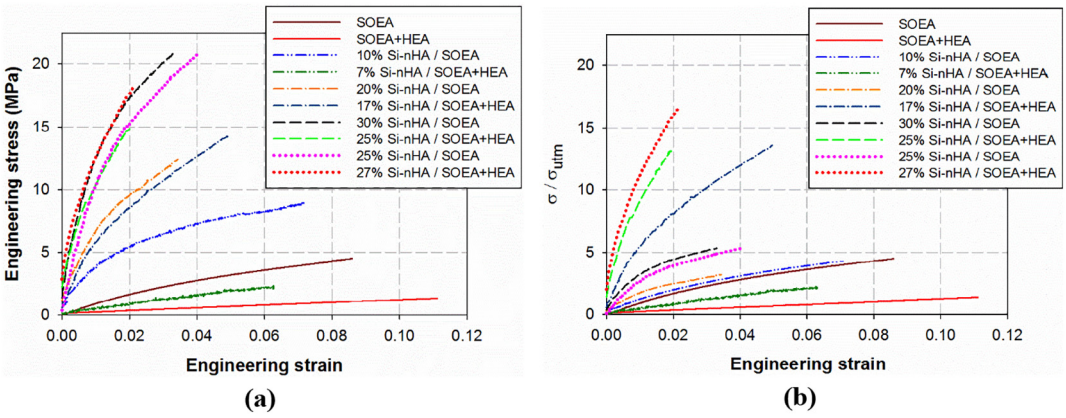

Fig. 6. Representative stress-strain curves from the specimen groups in this study; (a) engineering stress-strain curves; (b) engineering stress normalized by the ultimate tensile strength of each biopolymeric base resin versus engineering strain.

normalized stress-strain plots (Fig. 6(b)), by increasing Si-nHA volume fraction, the enhancement of strength in the SOEA + HEA nanocomposites are notably greater than those of the SOEA nanocomposites. Table 3 indicates the results of mechanical tests results of both resins and extruded nanocomposite filaments. Also, it can be seen in this table that by increasing Si-nHA volume fraction in the SOEA resin the toughness tends to be increased and its maximum value attained in 25% Si-nHA/SOEA. On the other hand, the maximum value of toughness in the SOEA + HEA based resin achieved in 17% Si-nHA/SOEA + HEA batch.

4.3. Predicted and experimental data comparisons

In this section, the Young's moduli (E_1) in the longitudinal direction for the extruded nanocomposite filaments are compared with 3D RVE results and the established Mori–Tanaka analytical model. It might be worth mentioning that we are currently limited to testing in tension along the filament axes, thus we were only able to extract E_1 experimentally.

Fig. 7(a) and (b) show E_1 versus various Si-nHA volume fractions extracted from experimental, numerical, and analytical results including (i) extruded Si-nHA/SOEA + HEA and Si-nHA/SOEA filaments using two different sizes of nozzle tip; (ii) 3D RVEs and (iii) Mori-Tanaka. As can be seen, the value of E_1 for SOEA + HEA approximately is 11 MPa and for SOEA is around 81 MPa. The value for the nHA nanoparticles is approximately 114,000 MPa [46]. Considering this very large range and the nano-scale of the particles, 3D RVE results and experimental data are very close and their trend is very similar. The Mori-Tanka model also correlates well, particularly at lower volume fractions; however, it has a different trend at higher volume fractions when compared with experimental and 3D RVE results. As can be seen in Fig. 7(c) and (d), the behavior and trend of each curve is very similar to the non-normalized curves. However, in the experimental data, at higher Si-nHA volume fractions, the normalized stiffness enhancement of SOEA + HEA is greater than for SOEA. This may be the result of improved dispersion and alignment due to the inclusion of HEA.

In order to further assess the capability of these two proposed nanocomposite inks, their properties were compared with the properties of other nominally bone-inspired materials reported in the literature. Table 4 reports the maximum value of Young's modulus and tensile strength of both nanocomposite inks proposed in this study as well as for the other bone-inspired materials reported in the literature. As can be seen in this table, the Young's modulus and tensile strength of SOEA + HEA/nHA are in the range of PCL/NH2, PCL/Collagen, and PLA/nHA. In addition, the Young's modulus of SOEA/nHA is greater than that of Chitosan/nBG while the strength is inferior.

5. General discussion

Natural and biological materials are thought to benefit from staggered structure in different length scales from the nano to the micro-scale [3–5]. Indeed, one of the primary goals of biomimicry is the development of staggered structures and its underlying mechanisms to simultaneously enhance the strength and toughness of such materials [3–5]. To this end, this study sought to produce two novel experimental nanocomposites by the compositing and extrusion of SOEA and rod-like nHA particles.

Fig. 6 presents representative stress-strain curves for the various nanocomposites tested in this study. Notably, the mechanical behavior of the SOEA + HEA based nanocomposites were more affected by the nHA particles and their increase in volume fraction. A relatively poor matrix (in terms of stiffness and strength) was notably strengthened, stiffened and perhaps even toughened by the inclusion of the nHA nanoparticles. This is presumably due to favorable interactions between the resin and the nanoparticles facilitated by inclusion of HEA, which

Table 3
Mean and standard deviation of the mechanical properties for the based resins and the extruded nanocomposite filaments having different Si-nHA volume fractions.

Material	E (MPa)	Tensile strength (MPa)	Tensile toughness (MJ m^{-3})
SOEA	81.7 ± 11.3	3.9 ± 0.3	(23 ± 5)*10^{-2}
SOEA + HEA	11.0 ± 0.1	1.0 ± 0.2	(8.3 ± 5)*10^{-2}
10% Si-nHA/SOEA	1125 ± 199	9.1 ± 0.4	(41 ± 7)*10^{-2}
7% Si-nHA/SOEA + HEA	156 ± 23	3.6 ± 0.7	(8.0 ± 8)*10^{-2}
20% Si-nHA/SOEA	2047 ± 200	14.0 ± 1.0	(24 ± 10)*10^{-2}
17% Si-nHA/SOEA + HEA	388 ± 25	14.1 ± 1.2	(42 ± 13)*10^{-2}
25% Si-nHA/SOEA	2602 ± 194	19.5 ± 1.8	(55 ± 15)*10^{-2}
25% Si-nHA/SOEA + HEA	534 ± 18	19.3 ± 4.0	(15 ± 12)*10^{-2}
30% Si-nHA/SOEA	3578 ± 191	22.8 ± 8.7	(43 ± 17)*10^{-2}
27% Si-nHA/SOEA + HEA	566 ± 21	20.4 ± 1.8	(20 ± 12)*10^{-2}

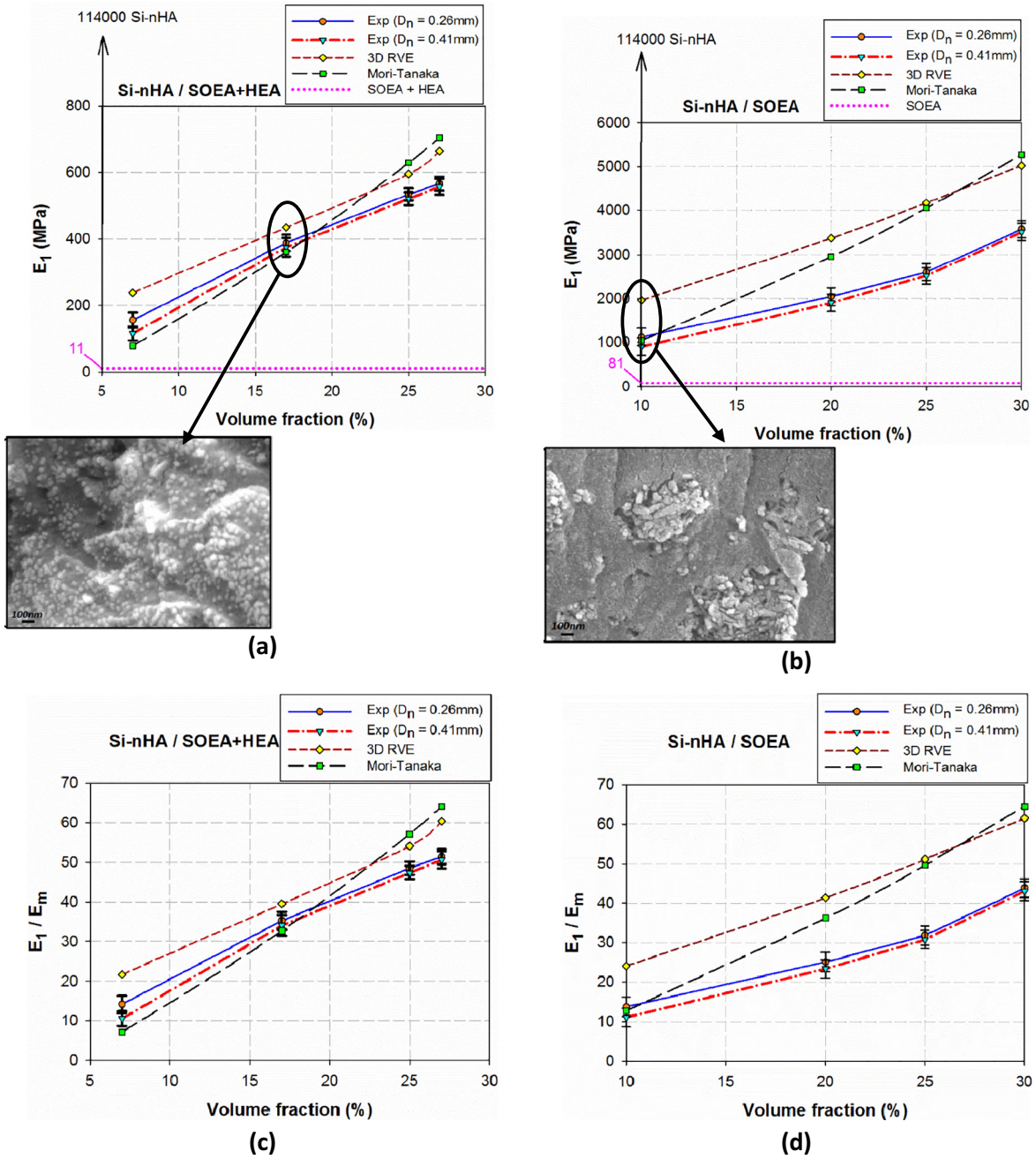

Fig. 7. Comparisons of Young's modulus and normalized Young's modulus versus nanoparticle volume fraction between experimental, 3D RVE, and Mori-Tanaka results. (a) and (b) are for the Si-nHA/SOEA + HEA nanocomposites; (c) and (d) are for the Si-nHA/SOEA nanocomposites.

can form hydrogen bonds with the nHA surface via its terminal hydroxyl group. Also, it was clearly evident that replacing some of the SOEA with HEA reduced the ink's viscosity (data not shown).

Overall, when comparing predictions from the two computational models to the experimental results, the 3D RVEs follow the same trend as nanoparticle volume fraction is increased but with an offset between the curves. Meanwhile, the Mori-Tanaka model did not follow the same trend. The reason for this divergence, especially for higher nanoparticle volume fractions, stems from assuming prolate spheroidal shaped inclusions instead of the real shape of the nHA nanoparticles as well as assuming non-realistic nanoparticle distribution. Previous studies reported inexactitudes with the Mori-Tanaka for higher inclusion volume fractions [64–66].

This suggests that, despite the offset, the 3D RVEs are better models of the elastic behavior of these nanocomposites since they can represent the particle dispersion and the inter-particle interactions. The offset is likely the result of error between the true elastic properties of the nano-hydroxyapatite particles (nHA) and those assumed in this work. The elastic properties of nHA presented in Section 3 and used in the models were found in the literature for hydroxyapatite with approximately the same degree of crystallinity [46]. Using the actual properties of the nHA particle would make the results more accurate and likely reduce the offset between the experimental and RVE curves. Unfortunately, mechanical testing of nano-scale hydroxyapatite particles is impractical at this time. Given the relatively small size of the offsets compared to the difference in moduli between the resin phase and the nHA, this error is reasonable and acceptable.

The greater offset between the experimental data and the RVE model for the SOEA-based nanocomposites, compared to the SOEA + HEA based nanocomposites, may be the result of poorer dispersion

Table 4
Comparisons of Young's modulus and tensile strength from the nanocomposite filaments in this study and other bone-inspired materials reported in the literature.

Composites	E (MPa)	Tensile strength (MPa)	Ref
Poly(ε-caprolactone) (PCL)/Continuous amine groups (NH2)	458.8	18.5	[49]
Poly(ε-caprolactone) (PCL)- Collagen	422.9	20.2	[49]
HYAFF/nHA	340	12	[50]
Poly(lactic acid) (PLA)/Tri-Calcium phosphate (α-TCP)	2.21	–	[51]
Poly(ε-caprolactone) (PCL)/nHA	21.9	0.9	[52]
HYAFF/Tri-calcium phosphate (α-TCP)	260	17	[53]
Poly(ε-caprolactone) (PCL)/Continuous amine groups (NH2)	550	24.2	[54]
Collagen – Poly(ε-caprolactone) (PCL)/nHA	1.73	–	[55]
Collagen-poly (lactic-co glycolic acid) (PLGA)/nHA	1200	9.7	[56]
Gelatin/nHA	412	4.4	[57]
Gelatin – Poly(ε-caprolactone) (PCL)/–nHA	23.5	3.7	[58]
Polyvinyl alcohol (PVA)-Gelatin/Biphasic calcium phosphate (nBCP)	8.4	–	[59]
Gelatin-Gellan/nHA	1.8	–	[60]
Chitosan–Polylactic acid (PLA)/nHA	704		[61]
Chitosan/Bioactive glass (nBG)	2600	49.6	[62]
Chitosan-Poly(lactic acid) (PLA)/nHA	880		[63]
SOEA/nHA	3578	22.8	Present work
SOEA-HEA/nHA	566	20.4	Present work

and alignment of the nHA. It is noted that the RVEs were developed assuming that all nanoparticles were aligned. Fig. 7 shows example images of the nanoparticles in the two nanocomposites. The SOEA-based nanocomposites presented more micro-scale agglomerations of nanoparticles. The SOEA + HEA nanocomposites regularly demonstrated finely dispersed nanoparticles. This is likely the result of improved chemical interactions between the HEA and the nanoparticles, including reduced viscosity. The greater increase in normalized stiffness with increasing volume fraction measured in the SOEA + HEA nanocomposites is likely also a result of the improved nHA dispersion and likely occurrence of alignment in some areas of the filament due to extrusion.

Given the above discussion, the 3D RVEs provided acceptable predictions of the elastic properties of the nano-composites; while their predictions for micro-scale inclusions were more reliable in a previous study [32]. This demonstrates the challenges in fabricating staggered nanostructures with simultaneous high mechanical performance, such as found in bone. Previously, these 3D RVE models were validated with micro-scale inclusions [32]. Therefore, the 3D RVE models can be a suitable reference model of non-uniformly dispersed and well aligned inclusions in composites at different length scales. In this study, dispersion and alignment may be the key factors leading to the differences found between the experimental and computational results.

6. Conclusions

Two novel bone-inspired nanocomposites with various nanoparticle volume fractions were extruded into filaments. These novel nanocomposites comprised of a vegetable oil-based resin (soybean oil epoxidized acrylate (SOEA)) or SOEA + 2-hydroxyethyl acrylate (HEA) which were reinforced using silanized nano-hydroxyapatite (Si-nHA). Tensile tests were conducted on both the resins. The SOEA was stronger and stiffer than the SOEA + HEA. Additionally, tensile tests were conducted on extruded nanocomposite filaments to extract their tensile stress-strain behavior. As the Si-nHA volume fraction was increased, the strength, stiffness, and toughness increased except for the highest Si-nHA volume fraction batches. By adding HEA to the SOEA, and consistent with our hypothesis, the viscosity decreased and dispersion and extrudability improved. This results in better particle alignment and relatively greater augmentation of filament mechanical properties relative to their base resins. Furthermore, several 3D FE micromechanical models (3D RVEs) and the well-established analytical model (Mori-Tanaka) were used based on phase material properties and volume fractions. The computed Young's modulus from these micromechanical models was compared with experimental data from both extruded nanocomposites. Results from the 3D RVE models were close to the experimental results, within acceptable tolerance due to the large phase moduli difference and the assumed modulus of the nHA. The 3D RVE approach better models the trends in modulus versus volume fraction than does the Mori-Tanaka analytical model. General differences in mechanical behavior between the two nanocomposite formulations were likely due to differences in nHA dispersion, where the addition of HEA seemed to improve dispersion and SOEA alone demonstrated some small agglomerations.

Acknowledgements

The authors thank the University of Waterloo and the Natural Sciences and Engineering Research Council of Canada (NSERC) for funding awarded to TLW and JM in support of this research. Also, the authors wish to thank all members of Composite Biomaterials Systems Lab at the University of Waterloo for their help in conducting the experiments. The authors thank Dr. Geng Li for his help in the numerical part of this paper and Professor Leonardo Simon for very helpful discussions regarding nanoparticle dispersion.

Data availability statement

The data required to reproduce these findings cannot be shared at this time as the data forms part of an ongoing study.

Appendix A

Table A1
Eshelby's tensor element for elliptical inclusions.

s_{11}	$4Q/3 + RI_3 + 2\rho^2 T$
$s_{22} = s_{33}$	$Q + RI_1 + 3T/4$
$s_{23} = s_{32}$	$Q/3 - RI_1 + 4T/3$
$s_{21} = s_{31}$	$-RI_1 - \rho^2 T$
$s_{12} = s_{13}$	$-RI_3 - T$
s_{44}	$Q/3 - RI_1 + T/4$
$s_{55} = s_{66}$	$2R - RI_1/2 + (1+\rho^2)T/4$
All other s_{ij}	0

$$I_1 = \frac{2\rho}{\sqrt{(\rho^2-1)^3}}\left(\rho\sqrt{\rho^2-1} - \cosh^{-1}(\rho)\right) \tag{A1}$$

$$Q = \frac{3}{8(1-\nu_m)} \tag{A2}$$

$$R = \frac{1-2\nu_m}{8(1-\nu_m)} \tag{A3}$$

$$T = Q\frac{4-3I_1}{3(\rho^2-1)} \tag{A4}$$

$$I_3 = 4-2I_1 \tag{A5}$$

Appendix B. Supplementary data

Supplementary data to this article can be found online at https://doi.org/10.1016/j.matdes.2019.107790.

References

[1] R.W. McCalden, J.A. McGeough, M.B. Barker, Age-related changes in the tensile properties of cortical bone. The relative importance of changes in porosity, mineralization, and microstructure, JBJS 75 (8) (1993) 1193–1205.
[2] R.B. Martin, J. Ishida, The relative effects of collagen fiber orientation, porosity, density, and mineralization on bone strength, J. Biomech. 22 (5) (1989) 419–426.
[3] R.O. Ritchie, The conflicts between strength and toughness, Nat. Mater. 10 (11) (2011) 817.
[4] U.G. Wegst, H. Bai, E. Saiz, A.P. Tomsia, R.O. Ritchie, Bioinspired structural materials, Nat. Mater. 14 (1) (2015) 23.
[5] A.R. Studart, Biological and bioinspired composites with spatially tunable heterogeneous architectures, Adv. Funct. Mater. 23 (36) (2013) 4423–4436.
[6] T. Bian, K. Zhao, Q. Meng, Y. Tang, H. Jiao, J. Luo, The construction and performance of multi-level hierarchical hydroxyapatite (HA)/collagen composite implant based on biomimetic bone Haversian motif, Mater. Des. 162 (2019) 60–69.
[7] B.G. Compton, J.A. Lewis, 3D-printing of lightweight cellular composites, Adv. Mater. 26 (34) (2014) 5930–5935.
[8] R.M. Erb, R. Libanori, N. Rothfuchs, A.R. Studart, Composites reinforced in three dimensions by using low magnetic fields, Science 335 (6065) (2012) 199–204.
[9] H. Le Ferrand, F. Bouville, T.P. Niebel, A.R. Studart, Magnetically assisted slip casting of bioinspired heterogeneous composites, Nat. Mater. 14 (11) (2015) 1172.
[10] E. Feilden, C. Ferraro, Q. Zhang, E. García-Tuñón, E. D'Elia, F. Giuliani, ... E. Saiz, 3D printing bioinspired ceramic composites, Sci. Rep. 7 (1) (2017) 13759.
[11] M.K. Hausmann, P.A. Rühs, G. Siqueira, J. Läuger, R. Libanori, T. Zimmermann, A.R. Studart, Dynamics of cellulose nanocrystal alignment during 3D printing, ACS Nano 12 (7) (2018) 6926–6937.
[12] G. Siqueira, D. Kokkinis, R. Libanori, M.K. Hausmann, A.S. Gladman, A. Neels, ... A.R. Studart, Cellulose nanocrystal inks for 3D printing of textured cellular architectures, Adv. Funct. Mater. 27 (12) (2017), 1604619.
[13] R. De Santis, V. Guarino, L. Ambrosio, Composite biomaterials for bone repair, Bone Repair Biomaterials, Woodhead Publishing 2019, pp. 273–299.
[14] R.Y. Basha, M. Doble, Design of biocomposite materials for bone tissue regeneration, Mater. Sci. Eng. C 57 (2015) 452–463.
[15] C. Zhang, T.F. Garrison, S.A. Madbouly, M.R. Kessler, Recent advances in vegetable oil-based polymers and their composites, Prog. Polym. Sci. 71 (2017) 91–143.
[16] S. Miao, P. Wang, Z. Su, S. Zhang, Vegetable-oil-based polymers as future polymeric biomaterials, Acta Biomater. 10 (4) (2014) 1692–1704.
[17] S. Miao, W. Zhu, N.J. Castro, M. Nowicki, X. Zhou, H. Cui, ... L.G. Zhang, 4D printing smart biomedical scaffolds with novel soybean oil epoxidized acrylate, Sci. Rep. 6 (2016), 27226.
[18] L. Quiles-Carrillo, S. Duart, N. Montanes, S. Torres-Giner, R. Balart, Enhancement of the mechanical and thermal properties of injection-molded polylactide parts by the addition of acrylated epoxidized soybean oil, Mater. Des. 140 (2018) 54–63.
[19] F.J. Martínez-Vázquez, M.V. Cabañas, J.L. Paris, D. Lozano, M. Vallet-Regí, Fabrication of novel Si-doped hydroxyapatite/gelatine scaffolds by rapid prototyping for drug delivery and bone regeneration, Acta Biomater. 15 (2015) 200–209.
[20] H. Lian, L. Zhang, Z. Meng, Biomimetic hydroxyapatite/gelatin composites for bone tissue regeneration: fabrication, characterization, and osteogenic differentiation in vitro, Mater. Des. 156 (2018) 381–388.
[21] W.Z. Yu, Y. Zhang, X. Liu, Y. Xiang, Z. Li, S. Wu, Synergistic antibacterial activity of multi components in lysozyme/chitosan/silver/hydroxyapatite hybrid coating, Mater. Des. 139 (2018) 351–362.
[22] H. Liu, T.J. Webster, Mechanical properties of dispersed ceramic nanoparticles in polymer composites for orthopedic applications, Int. J. Nanomedicine 5 (2010) 299.
[23] L. Wang, L. Weng, S. Song, Z. Zhang, S. Tian, R. Ma, Characterization of polyetheretherketone–hydroxyapatite nanocomposite materials, Mater. Sci. Eng. A 528 (10–11) (2011) 3689–3696.
[24] L. Wang, L. Weng, S. Song, Q. Sun, Mechanical properties and microstructure of polyetheretherketone–hydroxyapatite nanocomposite materials, Mater. Lett. 64 (20) (2010) 2201–2204.
[25] H. Ahmadian, M. Yang, A. Nagarajan, S. Soghrati, Effects of shape and misalignment of fibers on the failure response of carbon fiber reinforced polymers, Comput. Mech. (2018) 1–19.
[26] H. Ahmadian, B. Liang, S. Soghrati, An integrated computational framework for simulating the failure response of carbon fiber reinforced polymer composites, Comput. Mech. 60 (6) (2017) 1033–1055.
[27] G. Dai, L. Mishnaevsky Jr., Graphene reinforced nanocomposites: 3D simulation of damage and fracture, Comput. Mater. Sci. 95 (2014) 684–692.
[28] R. Wang, L. Zhang, D. Hu, C. Liu, X. Shen, C. Cho, B. Li, A novel approach to impose periodic boundary condition on braided composite RVE model based on RPIM, Compos. Struct. 163 (2017) 77–88.
[29] R. Wang, L. Zhang, D. Hu, X. Liu, C. Cho, B. Li, Progressive damage simulation in 3D four-directional braided composites considering the jamming-action-induced yarn deformation, Compos. Struct. 178 (2017) 330–340.
[30] G. Li, F. Sharifpour, A. Bahmani, J. Montesano, A new approach to rapidly generate random periodic representative volume elements for microstructural assessment of high volume fraction composites, Mater. Des. 150 (2018) 124–138.
[31] W. Xu, F. Wu, Y. Jiao, M. Liu, A general micromechanical framework of effective moduli for the design of nonspherical nano-and micro-particle reinforced composites with interface properties, Mater. Des. 127 (2017) 162–172.
[32] A. Bahmani, G. Li, T.L. Willett, J. Montesano, Three-dimensional micromechanical assessment of bio-inspired composites with non-uniformly dispersed inclusions, Compos. Struct. 212 (2019) 484–499.
[33] P. Comeau, T. Willett, Impact of side chain polarity on non-stoichiometric nano-hydroxyapatite surface functionalization with amino acids, Sci. Rep. 8 (1) (2018), 12700.
[34] C.Y.K. Lung, Z. Sarfraz, A. Habib, A.S. Khan, J.P. Matinlinna, Effect of silanization of hydroxyapatite fillers on physical and mechanical properties of a bis-GMA based resin composite, J. Mech. Behav. Biomed. Mater. 54 (2016) 283–294.
[35] N. Patel, S.M. Best, W. Bonfield, I.R. Gibson, K.A. Hing, E. Damien, P.A. Revell, A comparative study on the in vivo behavior of hydroxyapatite and silicon substituted hydroxyapatite granules, J. Mater. Sci. Mater. Med. 13 (12) (2002) 1199–1206.
[36] A.E. Porter, N. Patel, J.N. Skepper, S.M. Best, W. Bonfield, Comparison of in vivo dissolution processes in hydroxyapatite and silicon-substituted hydroxyapatite bioceramics, Biomaterials 24 (25) (2003) 4609–4620.
[37] N. Hijón, M.V. Cabanas, J. Pena, M. Vallet-Regí, Dip coated silicon-substituted hydroxyapatite films, Acta Biomater. 2 (5) (2006) 567–574.
[38] M. Vallet-Regí, D. Arcos, Silicon substituted hydroxyapatites. A method to upgrade calcium phosphate based implants, J. Mater. Chem. 15 (15) (2005) 1509–1516.
[39] A.M. Pietak, J.W. Reid, M.J. Stott, M. Sayer, Silicon substitution in the calcium phosphate bioceramics, Biomaterials 28 (28) (2007) 4023–4032.
[40] M. Wozniak, T. Graule, Y. de Hazan, D. Kata, J. Lis, Highly loaded UV curable nanosilica dispersions for rapid prototyping applications, J. Eur. Ceram. Soc. 29 (11) (2009) 2259–2265.
[41] M. Wozniak, Y. de Hazan, T. Graule, D. Kata, Rheology of UV curable colloidal silica dispersions for rapid prototyping applications, J. Eur. Ceram. Soc. 31 (13) (2011) 2221–2229.
[42] M.A. Sutton, J.J. Orteu, H. Schreier, Image Correlation for Shape, Motion and Deformation Measurements: Basic Concepts, Theory and Applications, Springer Science & Business Media, 2009.
[43] S.J. Eglen, D.D. Lofgreen, M.A. Raven, B.E. Reese, Analysis of spatial relationships in three dimensions: tools for the study of nerve cell patterning, BMC Neurosci. 9 (1) (2008) 68.
[44] R.W. Rodieck, The density recovery profile: a method for analysis of points in the plane applicable to retinal studies, Vis. Neurosci. 20 (3) (2003) 349.
[45] A. Bahmani, G. Li, T.L. Willett, J. Montesano, Three-dimensional microscopic assessment of randomly distributed representative volume elements for high fiber volume fraction unidirectional composites, Compos. Struct. 192 (2018) 153–164.
[46] A. Fritsch, L. Dormieux, C. Hellmich, J. Sanahuja, Mechanical behavior of hydroxyapatite biomaterials: an experimentally validated micromechanical model for elasticity and strength, J. Biomed. Mater. Res. A 88 (1) (2009) 149–161.
[47] T. Mura, Micromechanics of Defects in Solids, Springer Science & Business Media, 2013.
[48] M. Mirkhalaf, B. Ashrafi, A numerical study on improving the specific properties of staggered composites by incorporating voids, Mater. Today Commun. 13 (2017) 144–154.
[49] U. D'Amora, M. D'Este, D. Eglin, F. Safari, C.M. Sprecher, A. Gloria, ... L. Ambrosio, Collagen density gradient on three-dimensional printed poly (ε-caprolactone) scaffolds for interface tissue engineering, J. Tissue Eng. Regen. Med. 12 (2) (2018) 321–329.
[50] C. Giordano, V. Sanginario, L. Ambrosio, L.D. Silvio, M. Santin, Chemical-physical characterization and in vitro preliminary biological assessment of hyaluronic acid benzyl ester-hydroxyapatite composite, J. Biomater. Appl. 20 (3) (2006) 237–252.
[51] V. Guarino, L. Ambrosio, The synergic effect of polylactide fiber and calcium phosphate particle reinforcement in poly ε-caprolactone-based composite scaffolds, Acta Biomater. 4 (6) (2008) 1778–1787.
[52] F. Causa, P.A. Netti, L. Ambrosio, G. Ciapetti, N. Baldini, S. Pagani, ... A. Giunti, Poly-ϵ-caprolactone/hydroxyapatite composites for bone regeneration: in vitro characterization and human osteoblast response, J. Biomed. Mater. Res. A 76 (1) (2006) 151–162.
[53] V. Sanginario, M.P. Ginebra, K.E. Tanner, J.A. Planell, L. Ambrosio, Biodegradable and semi-biodegradable composite hydrogels as bone substitutes: morphology and mechanical characterization, J. Mater. Sci. Mater. Med. 17 (5) (2006) 447–454.
[54] A. Gloria, F. Causa, T. Russo, E. Battista, R. Della Moglie, S. Zeppetelli, ... L. Ambrosio, Three-dimensional poly (ε-caprolactone) bioactive scaffolds with controlled structural and surface properties, Biomacromolecules 13 (11) (2012) 3510–3521.
[55] J. Venugopal, P. Vadgama, T.S. Kumar, S. Ramakrishna, Biocomposite nanofibres and osteoblasts for bone tissue engineering, Nanotechnology 18 (5) (2007), 055101.
[56] S. Liao, F. Watari, Y. Zhu, M. Uo, T. Akasaka, W. Wang, ... F. Cui, The degradation of the three layered nano-carbonated hydroxyapatite/collagen/PLGA composite membrane in vitro, Dent. Mater. 23 (9) (2007) 1120–1128.
[57] X. Liu, L.A. Smith, J. Hu, P.X. Ma, Biomimetic nanofibrous gelatin/apatite composite scaffolds for bone tissue engineering, Biomaterials 30 (12) (2009) 2252–2258.
[58] A. Hamlekhan, F. Moztarzadeh, M. Mozafari, M. Azami, N. Nezafati, Preparation of laminated poly (ε-caprolactone)-gelatin-hydroxyapatite nanocomposite scaffold bioengineered via compound techniques for bone substitution, Biomatter 1 (1) (2011) 91–101.
[59] N.T. Ba Linh, K.H. Lee, B.T. Lee, Functional nanofiber mat of polyvinyl alcohol/gelatin containing nanoparticles of biphasic calcium phosphate for bone regeneration in rat calvaria defects, J. Biomed. Mater. Res. A 101 (8) (2013) 2412–2423.
[60] N. Barbani, G.D. Guerra, C. Cristallini, P. Urciuoli, R. Avvisati, A. Sala, E. Rosellini, Hydroxyapatite/gelatin/gellan sponges as nanocomposite scaffolds for bone reconstruction, J. Mater. Sci. Mater. Med. 23 (1) (2012) 51–61.
[61] X. Cai, H. Tong, X. Shen, W. Chen, J. Yan, J. Hu, Preparation and characterization of homogeneous chitosan–polylactic acid/hydroxyapatite nanocomposite for bone tissue engineering and evaluation of its mechanical properties, Acta Biomater. 5 (7) (2009) 2693–2703.
[62] J. Mota, N. Yu, S.G. Caridade, G.M. Luz, M.E. Gomes, R.L. Reis, ... J.F. Mano, Chitosan/bioactive glass nanoparticle composite membranes for periodontal regeneration, Acta Biomater. 8 (11) (2012) 4173–4180.

[63] X. Cai, H. Tong, X. Shen, W. Chen, J. Yan, J. Hu, Preparation and characterization of homogeneous chitosan–polylactic acid/hydroxyapatite nanocomposite for bone tissue engineering and evaluation of its mechanical properties, Acta Biomater. 5 (7) (2009) 2693–2703.
[64] M.H. Datoo, Mechanics of Fibrous Composites, Springer Science & Business Media, 2012.
[65] A.H. Akbarzadeh, A. Abedini, Z.T. Chen, Effect of micromechanical models on structural responses of functionally graded plates, Compos. Struct. 119 (2015) 598–609.
[66] A. Abedini, Z.T. Chen, A micromechanical model of particle-reinforced metal matrix composites considering particle size and damage, Comput. Mater. Sci. 85 (2014) 200–205.